Nonlinear Oscillations Induced by Follower Forces in Prestressed Clamped Rods Subjected to Drag

Soheil Fatehiboroujeni
Department of Mechanical Engineering,
University of California,
Merced, CA 95343
e-mail: sfatehiboroujeni@ucmerced.edu

Arvind Gopinath
Department of Bioengineering,
Health Science Research Institute,
University of California,
Merced, CA 95343
e-mail: agopinath@ucmerced.edu

Sachin Goyal
Department of Mechanical Engineering,
Health Science Research Institute,
University of California,
Merced, CA 95343
e-mail: sgoyal2@ucmerced.edu

Elastic-driven slender filaments subjected to compressive follower forces provide a synthetic way to mimic the oscillatory beating of biological flagella and cilia. Here, we use a continuum model to study the dynamical, nonlinear buckling instabilities that arise due to the action of nonconservative follower forces on a prestressed slender rod clamped at both ends and allowed to move in a fluid. Stable oscillatory responses are observed as a result of the interplay between the structural elastic instability of the inextensible slender rod, geometric constraints that control the onset of instability, energy pumped into the system by the active follower forces, and motion-driven fluid dissipation. Initial buckling instabilities are initiated by the effect of the follower forces and inertia; fluid drag subsequently allows for the active energy pumped into the system to be dissipated away and results in self-limiting amplitudes. By integrating the equations of equilibrium and compatibility conditions with linear constitutive laws, we compute the critical follower forces for the onset of oscillations, emergent frequencies of these solutions, and the postcritical nonlinear rod shapes for two forms of the drag force, namely linear Stokes drag and quadratic Morrison drag. For a rod with fixed inertia and drag parameters, the minimum (critical) force required to initiate stable oscillations depends on the initial slack and weakly on the nature of the drag force. Emergent frequencies and the amplitudes poston-set are determined by the extent of prestress as well as the nature of the fluid drag. Far from onset, for large follower forces, the frequency of the oscillations can be predicted by evoking a power balance between the energy input by the active forces and the dissipation due to fluid drag. [DOI: 10.1115/1.4041681]

1 Introduction

Stability analyses of slender structures subjected to follower loads are important instantiations of nonconservative problems in the theory of elastic stability. A number of thorough surveys of the developments and achievements on the structural stability of nonconservative systems can be found in the literature [1–3]. Conservative loads such as gravitational or electrostatic forces can be written as gradient of a time-independent potential function [4]. Nonconservative loads, however, do not fit this criterion; their magnitude and direction depend on the configuration of a structure (e.g., deflection and slope), its velocity, and time. Viscous damping is a well-known example of a nonconservative force, which depends on the velocity of a structure. Follower forces are a second type of nonconservative force which, acting either as a point force or a distributed load, always orient tangential to the deflection curve of a structure. Reut [5], Pfluger [6], Leipholz [4], and Beck [7] were among the first researchers to analyze the buckling of cantilevers subjected to follower forces.

In terms of applications, follower forces or variants thereof play a crucial role in many settings including pipes conveying fluid [8,9], self-thrust propelled structures [10], and rockets [11]. It is shown that equations for the response of disk-brake systems [12] can be mapped to the equations that govern the stability of Leipholz column [4]. More recently, follower forces have also been studied at smaller scales in microfluidic settings where inertia is negligible. For instance, synthetic filaments comprised of connected beads when actuated are observed to mimic the oscillatory beating of flagella and cilia [13,14]. Similarly, tunable colloidal chains assembled from chemically tailored Janus particles with controllable polarities can also be tuned to generate oscillatory beating [15–17]. While the length scales are very small in these applications (ranging from around 1–500 μm) when compared with those in more industrial settings, dynamical principles underlying their structural stability remain similar. Indeed connections between mechanics at multiple length scales have been illustrated in other biological settings [18–25].

Continuum models have been previously shown to be effective tools for analyzing the post-buckling behavior of slender inextensible active and inactive filaments subjected to shearing and/or compressive follower forces [17,21,26]. A crucial ingredient in these analyses is the dissipation of energy due to viscous drag; this dissipation provides a means to sustain steady oscillations with finite amplitudes. Furthermore, in zero inertia settings, the dissipation rate (and not inertia) provides the time scales controlling the temporal characteristics of the post-buckled state such as the steady-state beating frequency [17,26–28].

These studies have, however, focused on the buckling dynamics of free–free, fixed-free, and pinned-free filaments with the base state being a straight nonstressed filament or rod. The role of prestress in emergent oscillations driven by active distributed follower forces is yet to be elucidated. Here, we focus on the complementary scenario of a fixed–fixed rod—that is, a rod clamped at both ends and prestressed by decreasing the end-to-end distance, thereby generating a buckled shape and then subjected to a constant density follower force. This scenario has potential bio-inspired applications in which the interplay between geometry, elasticity, dissipation, and activity can be harvested to move and

Contributed by the Design Engineering Division of ASME for publication in the Journal of Computational and Nonlinear Dynamics. Manuscript received March 19, 2018; final manuscript received September 30, 2018; published online October 29, 2018. Assoc. Editor: Anindya Chatterjee.

manipulate fluid at various length scales. In the fixed-free scenario, the lack of constraint at the free-end allows for either lateral oscillations or steady rotations to develop in favorable conditions [17]. In our fixed–fixed scenario, the slack generated upon initial compression offers the necessary degree-of-freedom to allow for oscillations. The simulations are three-dimensional, but, by introducing strictly planar perturbations and loads, the oscillations remain planar. This protocol was adopted after observing that even in the presence of three-dimensional perturbations, for a given prestress value up to a certain limit, if the two-dimensional buckling shape is a stable equilibrium, the oscillations due to follower load remain planar. In other words, we have observed that in fixed–fixed scenarios, if the prestress value is close enough but yet smaller than the value required to destabilize the two-dimensional buckling shape to out-of-plane mode, then starting from a two-dimensional stable shape can still result into out-of-plane oscillations. This will be the subject of scrutiny in a sequel paper.

2 Model

We consider a rod that is in stress-free state when maintaining a straight shape. By moving one of the clamped ends of the rod toward the other end and forcing the rod to bend due to bucking as shown in Fig. 1(*a*), we generate prestress in the rod. Thus, prestress rate is controlled by the end-to-end length of the rod, $L_{ee} < L$.

The continuum rod model that we use [24] follows the classical approach of the Kirchhoff [29], which assumes each cross section of the rod to be rigid. We work in a lab-fixed Cartesian coordinate system and use subscripts to denote components. The rigid-body motion of individual cross section is examined by discretizing an elastic rod into infinitesimal elements along its arc length. The position and orientation of each cross section are determined in space s (i.e., the arc-length variable) and time t by tracking the transformation of a body-fixed frame $\hat{a}_i(s,t)$ with respect to an inertial frame of reference $\hat{e}_i(s,t)$ as shown in Fig. 1(*b*).

Vector $\mathbf{R}(s,t)$ defines the position of the cross section relative to the inertial frame of reference. The spatial derivative of $\mathbf{R}(s,t)$ is denoted by vector $\mathbf{r}(s,t)$. Deviation of $\mathbf{r}(s,t)$ from the unit normal of the cross section determines shear while the change in its magnitude quantifies stretch (extension or compression) along the arc length s. Both shear and stretch deformations are negligible for filaments with large slenderness (length/thickness) ratio under compression. So, we assume $\mathbf{r}(s,t) = \hat{a}_3(s,t) = \hat{t}(s,t)$, where $\hat{t}(s,t)$ is the unit tangent vector along the arc length. Vector $\boldsymbol{\kappa}(s,t)$ captures two-axes bending and torsion of the rod, and vectors $\mathbf{v}(s,t)$ and $\boldsymbol{\omega}(s,t)$ represent the translational velocity and the angular velocity of cross section, respectively. The stress distribution over the cross section of the rod results in a net internal force and a net internal moment shown, respectively, with $\mathbf{f}(s,t)$ and $\mathbf{q}(s,t)$.

2.1 Governing Equations. The equations of equilibrium (1) and (2) are derived by applying Newton's second law to an infinitesimal element of the rod. The compatibility Eqs. (3) and (4) follow from the space–time continuity of the cross section position $\mathbf{R}(s,t)$, and the space–time continuity of the transformation from $\hat{a}_i(s,t)$ to $\hat{e}_i(s,t)$

$$m\left(\frac{\partial \mathbf{v}}{\partial t} + \boldsymbol{\omega} \times \mathbf{v}\right) - \left(\frac{\partial \mathbf{f}}{\partial s} + \boldsymbol{\kappa} \times \mathbf{f}\right) - \mathbf{F} = \mathbf{0} \tag{1}$$

$$\underline{\mathbf{I_m}}\,\frac{\partial \boldsymbol{\omega}}{\partial t} + \boldsymbol{\omega} \times \underline{\mathbf{I_m}}\,\boldsymbol{\omega} - \left(\frac{\partial \mathbf{q}}{\partial s} + \boldsymbol{\kappa} \times \mathbf{q}\right) + \mathbf{f} \times \mathbf{r} - \mathbf{Q} = \mathbf{0} \tag{2}$$

$$\frac{\partial \mathbf{r}}{\partial t} + \boldsymbol{\omega} \times \mathbf{r} - \left(\frac{\partial \mathbf{v}}{\partial s} + \boldsymbol{\kappa} \times \mathbf{v}\right) = \mathbf{0} \tag{3}$$

$$\frac{\partial \boldsymbol{\kappa}}{\partial t} - \left(\frac{\partial \boldsymbol{\omega}}{\partial s} + \boldsymbol{\kappa} \times \boldsymbol{\omega}\right) = \mathbf{0} \tag{4}$$

In Eqs. (1)–(4), all derivatives are relative to the body-fixed reference frame, m is the mass of the rod per unit length, and $\underline{\mathbf{I_m}}$ is a 3-by-3 tensor of the moments of inertia per unit length. External force per unit length $\mathbf{F}$ as well as the external moment per unit length $\mathbf{Q}$ captures interactions of the rod with the environment such as drag force.

The distributed follower forces and moments in this model are captured by $\mathbf{F}$ and $\mathbf{Q}$. In the scenario of fixed–fixed rod, we consider the effect of distributed follower forces in tangential direction (along $\hat{a}_3(s,t)$) in this paper. Henceforth, for simplicity of notation, we refer to this tangential follower force density by

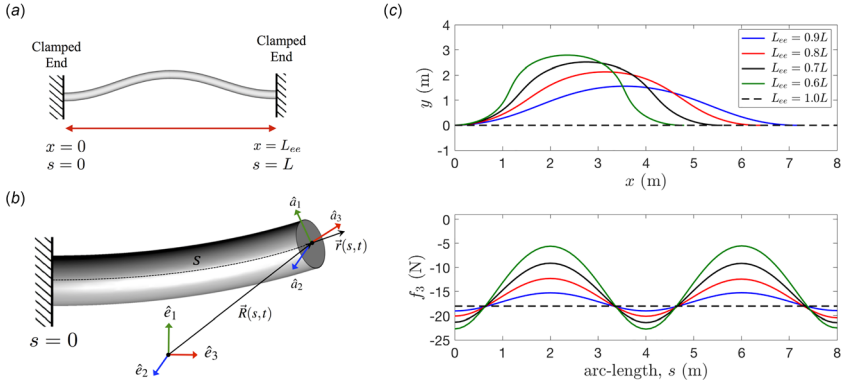

Fig. 1 (*a*) Schematic representation of a rod of unstressed length *L* with fixed–fixed boundary condition (clamped at both ends). The end-to-end distance when buckled is $L_{ee} < L$. (*b*) The motion of material points comprising the cross section of the rod at arc-length position, *s* and at time *t* is determined by tracking the transformations of the body-fixed frame $\hat{a}_i(s,t)$ with respect to the inertial frame of reference $\hat{e}_i$. (*c*) The shape (top) and prestress (bottom) in the buckled state for different values of L_{ee}/L. The dashed line corresponds to the unbuckled case $L_{ee}/L = 1.0$. Prestress here is defined as the component of the internal force in the direction of cross-sectional normal vector $\hat{a}_3(s,t)$ i.e., f_3. Here, we use the tension along the filament, f_3, to characterize prestress. For the shapes we study in this paper, there is a one-to-one correspondence between the two.

scalar F. In the scenario of fixed-free rods, there may also be point follower loads at one of the boundaries.

To close and solve the equilibrium and compatibility (1)–(4) equations, we need a constitutive law relating the deformations to the restoring forces. We choose to use the constitutive law for an isotropic and linearly elastic rod; this takes the form of an algebraic relationship

$$\mathbf{q}(s,t) = \underline{\mathbf{B}}(s)\boldsymbol{\kappa}(s,t) \tag{5}$$

The matrix $\underline{\mathbf{B}}$ in Eq. (5) encodes the bending and torsional stiffness moduli of the rod. By choosing the body-fixed frames of reference to coincide with principal axes of rod cross section, $\underline{\mathbf{B}}$ can be written as

$$\underline{\mathbf{B}} = \begin{bmatrix} EI_1 & 0 & 0 \\ 0 & EI_2 & 0 \\ 0 & 0 & GI_3 \end{bmatrix} \tag{6}$$

where E is the Young's modulus, G is the shear modulus, and I_1, I_2, and I_3 represent the second moment of area of the rod's cross section about its principal axes. Our choice, as implicit in Fig. 1(*b*), implies that subscripts $i = 1, 2$ in $\hat{a}_i(s,t)$ represent the rod's axes of bending and $i = 3$ represents torsional axis.

2.2 Numerical Scheme. The generalized-α method [30] is adopted to compute the numerical solution of this system, subjected to necessary and sufficient initial and boundary conditions. A detailed description of this numerical scheme applied to this formulation is given in the extant literature [25]. The important feature of this method is that it is an unconditionally stable second-order accurate method for numerically stiff problems, which allows for controllable numerical dissipation. In the context of rod mechanics, it brings an improvement over box method [31] by controlling the Crank–Nicolson noise, in which numerical solution oscillates about the true solution at every (temporal or spatial step) and corrupts the subsequent computation. The numerical formulation that is used here is previously benchmarked with experimental data for modeling both in-plane and out-of-plane buckling of slender rods [25,32]. We chose the value of shooting method iterations, i.e., the error in the norm of a vector containing state variables, at each time-step to be 10^{-9} to ensure the convergence of numerical integrations in time. Observing a stable (steady-state) oscillation is also an indirect way to elicit the sanity of numerical simulations.

While in the analysis presented here, the constitutive equations as embodied in Eqs. (5) and (6) are linear and local, the method can be adapted to analyze problems where the constitutive relationships are nonlinear and nonlocal [33].

2.3 Forms for the Fluid Drag. We analyze fluid effects arising from two types of drag forces, namely Stokes drag [S] and Morrison drag [M] given in Eqs. (7) and (8), respectively, and as also explained in Ref. [34]

$$\mathbf{F}_{\mathrm{S}} = -\frac{1}{2}\rho_{\mathrm{f}} d\left(C_n \hat{t} \times (\mathbf{v} \times \hat{t}) + \pi C_t (\mathbf{v} \cdot \hat{t})\hat{t}\right) \tag{7}$$

$$\mathbf{F}_{\mathrm{M}} = -\frac{1}{2}\rho_{\mathrm{f}} d\left(C_n |\mathbf{v} \times \hat{t}| \hat{t} \times (\mathbf{v} \times \hat{t}) + \pi C_t (\mathbf{v} \cdot \hat{t}) |\mathbf{v} \times \hat{t}| \hat{t}\right) \tag{8}$$

In both equations, ρ_{f} and d represent the environment fluid density and diameter of the rod, respectively. Drag coefficients (per unit length) C_n and C_t are given in Table 1. In typical scenarios, the normal drag coefficient is larger than the tangential coefficient, i.e., $C_n > C_t$. For the nonlinear form of the Morrison drag, motivated by filament motions corresponding to high Reynolds number, $C_n/C_t \gg 1$. We note that the Stokes [S] form for the drag is linear in the velocity while the Morrison form [M] is quadratic, and hence nonlinear in the velocity. Thus, for the same change in configuration and frequency, the Morrison form will result in a larger viscous dissipation per unit length than the Stokes form. Conversely, if we require that the same amount of energy be dissipated, the Stokes limit will be characterized by either higher frequency or by larger amplitude deformations or both.

Table 1 Numerical values for the geometric and elastic rod properties and drag coefficients used in the computations. The ratio $C_n/\pi C_t = 3.18$ is comparable to the value 2 for the limit of purely viscous (Stokesian) drag ratio for a slender rod using resistivity theory [19].

Quantity	Variable	Value	Units
Diameter	d	0.0096	m
Length	L	8	m
Mass per unit length	m	0.2019	kg/m
Young's modulus	E	68.95	GPa
Shear modulus	G	27.58	GPa
Second moment of area	$I_1 = I_2$	4.24×10^{-10}	m^4
Polar moment of area	I_3	8.48×10^{-10}	m^4
Normal drag coefficient	C_n	0.1	m s or m^2
Tangential drag coefficient	C_t	0.01	m s or m^2
Surrounding fluid density	ρ_{f}	1000	$\mathrm{kg/m}^3$

Before we proceed to the discussion of results, we would like to bring the reader's attention to two important features. First, in the Stokes limit when the rod moves in a Newtonian fluid, the normal and tangential drag coefficients are independent of density, only weakly dependent on the diameter of the rod d and proportional to fluid viscosity. Here, in order to treat linear and nonlinear fluid drag in a consistent framework, we set the values of these drag coefficients to constants and focus solely on the role of activity (embodied in the follower force density) and the prestress (embodied in the ratio L_{ee}/L). Second, rod inertia (solid inertia due to the mass density of the rod) is not zero. In the absence of fluid drag that allows for a dissipative mechanism, the rod will undergo buckling instabilities under the action of follower forces and subsequent shapes will be characterized by increasing amplitude (with time). Dissipation due to the fluid drag however will limit the amplitude of the oscillations and also control the emergent frequencies. All simulations were conducted with m, rod geometry, rod length, and elastic properties and fluid density held fixed. The only parameters allowed to vary were L_{ee} and $|F|$.

3 Results

We begin by present results for the critical value of the follower force density F_{cr} versus end-to-end distance L_{ee}/L and then, following that, explore how the beating frequency, $\omega(|F|, L_{\mathrm{ee}}/L)$ both at the critical point and for values of the follower force $|F| > F_{\mathrm{cr}}$ depends on the prestress. In all cases, a cylindrical rod with slenderness ratio of 800 is simulated with properties given in Table 1.

3.1 Benchmark: Critical Force for Beck's Column. In order to benchmark the model presented in this paper, we calculate the critical buckling force for the Beck's column comprising a fixed-free cantilever with a uniformly distributed mass and subject to a compressive point load that is always tangential to the free-end of the column. Beck's analysis, published in German [7] and reviewed in English [2], yields the following expression for the critical buckling force, P_{cr} of a cantilever with bending stiffness, EI and length, L in absence of damping dissipation, $P_{\mathrm{cr}} \approx 20.05\ (EI/L^2)$.

Using the formulation presented in Sec. 2, we investigate the value of the critical buckling force for Beck's column and compare it to this value reported in the literature. To approach the conditions of a quasi-static simulation and reduce the dynamic effects, we apply a compressive follower force, which gradually

increases in time, to the free end of the cantilever. The critical force found by our computational model in absence of viscous drag is approximately $P_{cr} \approx 20.10\ (EI/L^2)$, which is within 3% of the exact value.

3.2 Critical Points and Effect of Fluid Drag on Stability. In this section, we present the results for the post-buckling analysis of prestressed rods with fixed–fixed boundary conditions for various values of the slack (and thus, various values of the prestress as well as base curvature). Identifying and characterizing critical points as well as the force–frequency relationship is crucial to designing accurately controllable oscillations.

3.2.1 Stability Boundary: Prestressed Versus Stress-Free Base States. We obtain the base state by starting with a straight fixed–fixed rod with clamps at both ends and then move one of the clamped ends of the rod toward the other end. This process generates prestress in the rod c.f., Fig. 1(*a*), and thus correspondingly, prestress values can be controlled by the end-to-end length of the rod, L_{ee} as shown in Fig. 1(*c*). Starting from this base state completely determined by the ratio L_{ee}/L, we then apply uniformly distributed follower load, $F\hat{a}_3$ along the rod and integrate the rod equations in time.

We compute the critical points (or critical follower force density) by numerically integrating the time-dependent Eqs. (1)–(8) and seeking the point at which stable oscillations emerge. This is done for varying values of the slack $1 - L_{ee}/L$. Our aim being the identification of parameter ranges that can be exploited experimentally, we focus our attention on slack values satisfying $L_{ee}/L < 0.9$.

When the magnitude of the follower load, $|F| > F_{cr}$, buckled shapes become unstable and beating oscillations emerge. Based on our results, we surmise that these oscillatory solutions bifurcate from the static bent solution via Hopf–Poincare bifurcations; this mechanism is akin to that observed in the free-clamped case. In Fig. 2, we show the magnitudes of the critical follower load F_{cr} against the slack $1 - L_{ee}/L$ for both types of drag forces. We find, surprisingly, that for $0.05 < 1 - L_{ee}/L < 0.5$, the critical value increases in magnitude as the extent of prestress in the rod increases even though increasing $1 - L_{ee}/L$ implies more slack. The magnitude of critical follower load found to be nearly the same for both Stokes and Morrison drags (discrepancies being $< 2\%$).

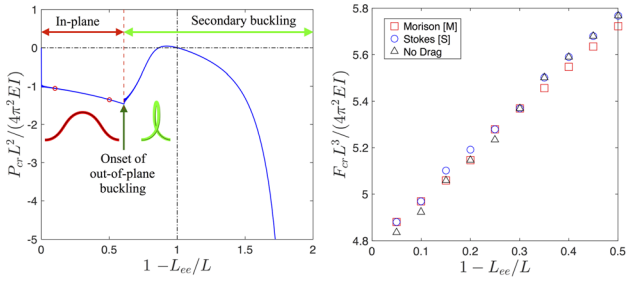

Fig. 2 (Left) A measure of the prestress may be gained by examining the plot of $f_3(L)$ versus $1 - L_{ee}/L$. The results of this paper focus on the range $0.05 < 1 - L_{ee}/L < 0.5$ shown between the two markers (red circles). (Right) Critical load for onset of oscillations F_{cr} versus scaled decrease in end-to-end distance $1 - L_{ee}/L$ for both Stokes [S] drag and Morrison [M] drag. We note that the critical loads are roughly the same for the two forms of fluid drag and deviate little from the nondrag value. This is not surprising for the Morrison drag [M] as it is nonlinear and hence does not enter the linear stability equations at leading order for small perturbations. Given that the Stokes [S] values are close to the no drag values, we surmise that the onset of vibrations and onset of flutter are very close to one another for the parameter range investigated. For $0.05 < 1 - L_{ee}/L < 0.5$, the critical force F_{cr} increases as $1 - L_{ee}/L$, or prestress, increases. For the region $1 - L_{ee}/L < 0.05$, we are unable to obtain well-defined results since the slack is very small in this region and inextensibility constraint makes the problem very stiff necessitating very small time intervals. Since the focus of our paper is to investigate the role of slack (prestress), we choose to study values of $L_{ee}/L < 0.9$.

Previous studies have demonstrated that the stability of a nonconservative system involving time derivatives (of any order) can be obtained using a dynamic criterion of stability in which the growth rates of infinitesimal perturbations are analyzed. We note that inertial terms are second order in time (but linear), the Stokes drag is effectively first order in time (and linear as well). The Morrison drag is, however, a nonlinear time derivative; therefore, at linear order, this drag will not enter the equations of motions. That is, if one analyzes the linear stability of a nonmoving base state satisfying (1)–(8) to small perturbations, the Morrison drag term will not enter the linear stability formulation while inertial drag and the Stokes drag will. We observe that the purely inertial, no-drag critical points predict the stability envelope reasonably well even when drag is included and fluid drag is seen to have only a small influence on the stability envelope for the parameters considered. However, a full linear stability analysis is required to tease out these effects and determine the differences between the purely inertial stability boundary and the boundary for rods with inertia and drag.

Some insight into the first effects of fluid drag on the stability boundary may be obtained by examining the competing effects of inertia and drag in an initially straight unstressed rod. Consider a Beck cantilever with bending stiffness EI clamped at $s = 0$ and subject to a constant follower force FL at $s = L$. The cantilever moves in a fluid that exerts a Stokes drag of the form Eq. (7). Taking the base state to be a straight stress-free rod, rewriting the equations in terms of the lateral displacement from the straight state, and retaining only linear terms, we find that $(0 \le s' \equiv s/L \le 1)$ the lateral displacement $H_\perp = LH$ satisfies

$$\varepsilon_I \frac{\partial^2 H}{\partial t^2} + \varepsilon_D \frac{\partial H}{\partial t} + \frac{\partial^4 H}{\partial s'^4} + \beta \frac{\partial^2 H}{\partial s'^2} = 0 \tag{9}$$

where $\beta \equiv FL^3/EI$, ε_I is a scaled inertia coefficient proportional to the mass density and ε_D is a scaled drag coefficient. The boundary conditions for the fixed-free cantilever are

$$H(0) = \frac{\partial H}{\partial s'}(0) = \frac{\partial^2 H}{\partial s'^2}(1) = \frac{\partial^3 H}{\partial s'^3}(1) = 0 \tag{10}$$

Solutions with (complex) growth rate Ω satisfy the boundary conditions at $s = 0$ provided they are of the form

$$\hat{H}(s') = a_1 e^{\Omega t}\left[\cosh(\lambda_1 s')\left(1 - \frac{\cos(\lambda_2 s')}{\cosh(\lambda_1 s')}\right)\right] + a_2 e^{\Omega t}\left[\sinh(\lambda_1 s')\left(1 - \frac{\lambda_1}{\lambda_2}\frac{\sin(\lambda_2 s')}{\sinh(\lambda_1 s')}\right)\right] \tag{11}$$

with associated dispersion relationships

$$\lambda_1^2 = \sqrt{\beta^2/4 - \Omega(\varepsilon_D + \varepsilon_I \Omega)} - \beta/2 \tag{12}$$

$$\lambda_2^2 = \sqrt{\beta^2/4 - \Omega(\varepsilon_D + \varepsilon_I \Omega)} + \beta/2 \tag{13}$$

In the absence of drag $\varepsilon_I = 1$ and $\varepsilon_D = 0$, solvability conditions result in the equation

$$1 + 2\left(\frac{\Omega}{\beta}\right)^2 (1 + \cosh\lambda_1 \cos\lambda_2) + \left(\frac{\Omega}{\beta}\right) \sinh\lambda_1 \sin\lambda_2 = 0 \tag{14}$$

At the critical point with $\beta = \beta_c$, the real part of Ω is zero so that $\Omega(\beta = \beta_c) = i\omega(\beta_c)$. Solving Eq. (14), we find that onset of instability is at the classical value $F_{cr} \approx 20.05\,(EI/L^3)$ first obtained in Ref. [7] see also Ref. [2]. The (undamped) critical flutter force density F_{cr} and the critical load $F_{cr}L$ are identified as the lowest forces at which a pair of imaginary eigenvalues coalesces solutions bifurcating via the classical Hopf–Poincare mechanism. The loss of stability in the case of conservative dead load corresponds to divergence with a single real eigenvalue crossing the real axis. With the follower force, the mechanism of stability loss corresponds to flutter.

In the complementary limit, when inertia is absent with $\varepsilon_I = 0$ and $\varepsilon_D = 1$, solvability requirements for a_1 and a_2 to be nontrivial yield

$$-2\left(\frac{\Omega}{\beta^2}\right)(1 + \cosh\lambda_1 \cos\lambda_2) + i\sqrt{\frac{\Omega}{\beta^2}}\sinh\lambda_1 \sin\lambda_2 = -1 \quad (15)$$

In this regime, the stability picture becomes richer. The onset of vibrations is first observed at Ref. [26] $\beta_{cr}\, L = 20.05$—however, the presence of fluid drag results in these oscillations being damped out. In other words, the response to disturbances is a decaying oscillation as the most dangerous eigenvalues are complex with a negative real part. At a higher value of the loading, second critical point is observed at $F_{cr} = P_{cr}/L \approx 37.69\ (EI/L^3)$ when the real part of the most dangerous eigenvalues vanishes and oscillations grow.

The more general case (with an unstressed base state and fluid drag) is the inertia-less fixed-free Leipholz column (cantilever) with a continuously distributed follower force. The linear stability of such a column with a stationary straight cantilever as the base state is governed by

$$\frac{\partial H}{\partial t} + \frac{\partial^4 H}{\partial s'^4} + \beta\frac{\partial}{\partial s'}\left((1 - s')\frac{\partial H}{\partial s'}\right) = 0 \quad (16)$$

Numerical results indicate that the straight rod yields to stable oscillations with a well-defined emergent frequency at $F_{cr} \approx 75.5\ (EI/L^3)$ [17], a value different from what we see for a stressed fixed–fixed column with Stokes drag.

Thus, for the stress-free scenario, fluid drag (that is linear in variables) influences the stability boundary and results in critical points (or the locus of critical points) that are different from those predicted purely from the nondrag, inertial set of equations.

3.2.2 Shapes Far From Criticality. Despite the low sensitivity of F_{cr} to the nature of drag law, beating configurations and the steady frequency of oscillations are found to be significantly different for Stokes and Morrison drags. This can be explained by the fact that Morrison drag dissipates energy at a higher rate compared to the Stokes drag for the same frequency and mode shapes.

Figures 3 and 4 illustrate how the shape of the rod (spatial-dependent curvature function) evolves during one complete oscillation for both Stokes [S] and Morrison [M] forms of fluid drag. We visually observe that configurations of the rod subjected to Stokes drag consist of multiple shape modes resulting in higher order harmonics—this is evident when the Fourier transform is analyzed as shown in Fig. 5. For rods subject to Morrison drag, higher order shapes are not recognizable visually. This is consistent with the Fourier transform; it is clear that higher order harmonics seen for oscillations in the Stokes case are not observed for the Morrison case.

3.3 Stable Oscillation Frequencies When $L_{ee}/L < 0.9$. The shapes of the rods illustrate one aspect of the dynamical state achieved—a second, equally important feature is the frequency of oscillations. This is related to the wave speed associated with the propagation of curvature along the arc length as the rods execute a cycle in configuration-time space. In all cases, the oscillations are tracked for 40 s, which corresponds to a minimum of 8 full oscillations up to a maximum of 70 full oscillations.

With the computational model used here, we systematically investigated the effect of prestress and the follower force on the frequency of oscillations near the critical point as well as far from the critical point where $|F - F_{cr}|/F_{cr} > 1$. Figures 6 and 7 illustrate the frequency of beating oscillations for rods under various end-to-end distances and subjected to both types of viscous drag. We observe that frequency of oscillations under Stokes drag—shown in Fig. 6—undergoes a sudden increase once the magnitude of the distributed follower load reaches a second critical limit. Such a behavior is absent when the drag follows the Morrison law. The frequency values are recast in log–log form in Fig. 7(*a*) and shown alongside the variation relating the frequency to the follower force magnitude, $\omega \sim |F|^{4/3}$ for an inertia-free cantilever subject to follower forces moving under Stokesian drag [17]. We

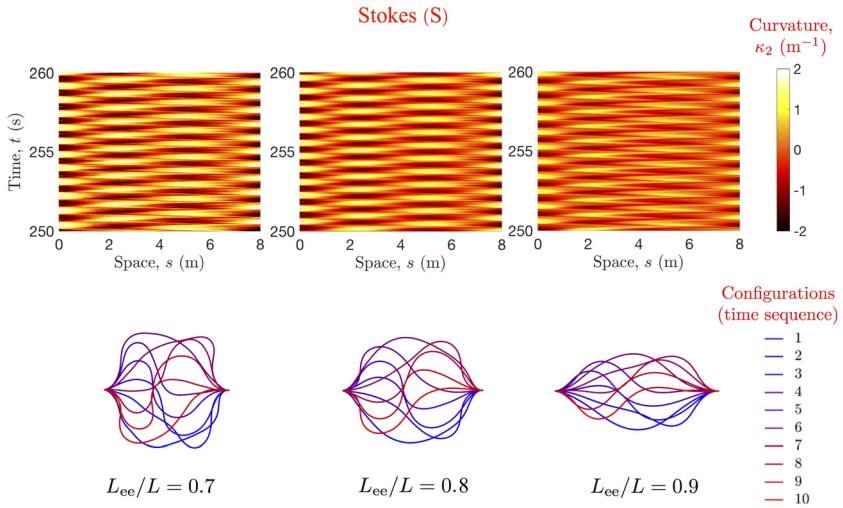

Fig. 3 Configurations of the oscillating rod when $|F| = 15$ N/m, when the drag force is of the Stokes [S] form. We show kymographs of the curvature in the top column, as well as the shapes over a period (labeled sequentially from 1–10) in the bottom column. We see increasingly sharper shapes (higher values of $|\kappa_2|$) for smaller values of L_{ee}/L.

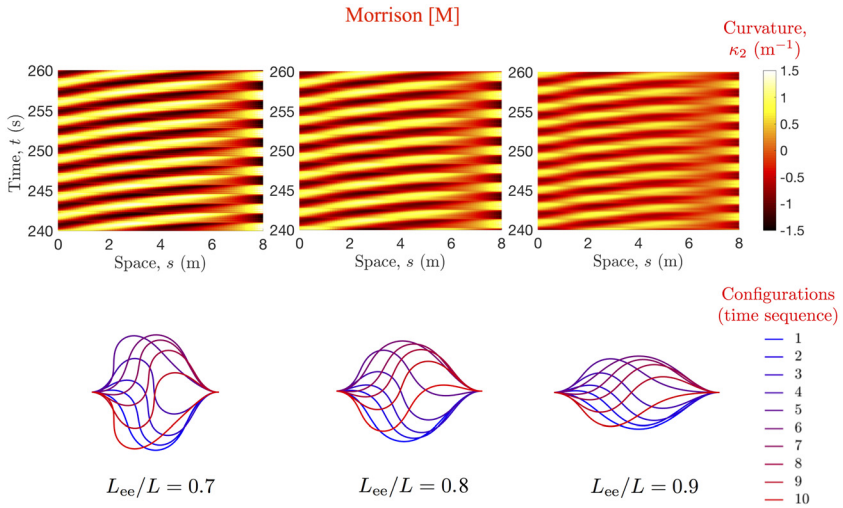

Fig. 4 Configurations of the oscillating rod when $|F| = 15$ N/m, when the drag force is of the Morrison [M] form. We show kymographs of the curvature in the top column, as well as the shapes over a period (labeled sequentially from 1–10) in the bottom column. As in the [S] case, we see increasingly sharper shapes (higher values of $|\kappa_2|$) for smaller values of L_{ee}/L. Furthermore, the shapes are smoother and the oscillations involve lower amplitudes than the corresponding shapes for the [S] case.

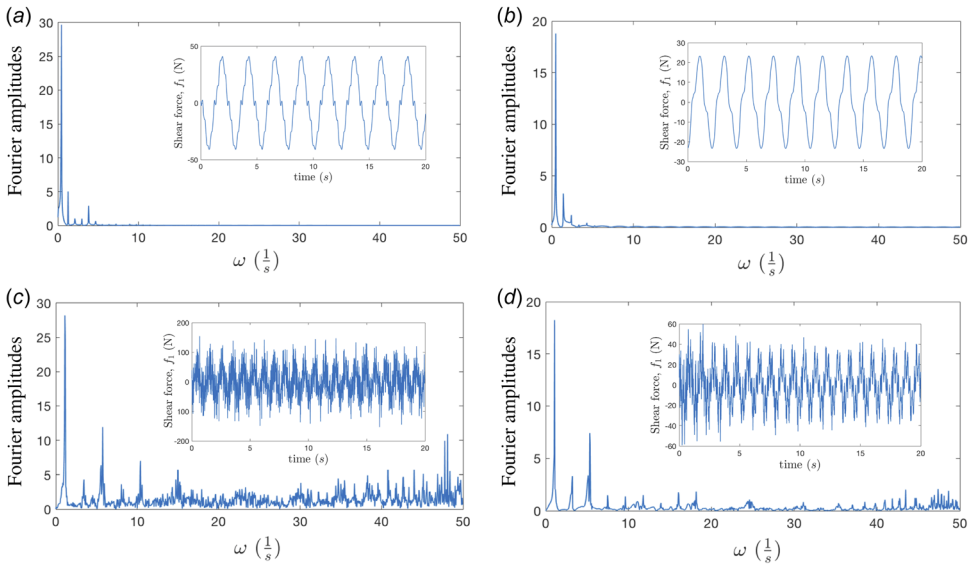

Fig. 5 Fourier transform (in the time domain) of the shear force at the midspan length of the rod shows that higher harmonics (insets show the raw data) are damped in the case of the nonlinear Morrison drag ((*a*) and (*b*)) more effectively than for the linear Stokes drag ((*c*) and (*d*)). The right column of the picture corresponds to $L_{ee}/L = 0.9$ while the left column corresponds to $L_{ee}/L = 0.7$. The ratio of drag coefficients for both cases is 3.18. Intuitively, we expect this ratio to affect the extent of dampening. The magnitude of $|F|$ for all cases is 14 N/m.

note that the frequencies we observe do not confirm to this scaling, due to the excitation of higher order shape modes and the effect of the prestress. In Fig. 8, we compare details of two points on the frequency–force curve, prior to and after the sudden (nonlinear) jump. Tracking the time evolution of internal shear force and calculating its Fourier transformation for points A and B of the Fig. 6 reveals that suppression of the higher oscillatory modes and concomitant change in the shapes (as manifested by localization of curvature) probably results in rapid increase in the steady-state frequency and a nonmonotonic nature of the curve.

Examining the force dependence of the beating filaments subject to Morrison type drag forces in Fig. 7(*b*), we identify two trends not evident in the Stokes case. First, the $\omega - |F|$ curves do not show any breaks but seem to be monotonic. Second, curves for various L_{ee}/L bunch together as $|F|/F_{cr} \gg 1$; indeed, the frequency seems flat for $|F| = 34\,\mathrm{N/m}$ when compared to the curve for 15 N/m. All these observations suggest that at least for the Morrison drag case, when we have large F or small L_{ee}/L, the effect of the slack and indeed of the boundary (end-to-end distance L_{ee} becomes negligible. Instead, the distance over which curvature is concentrated (localized) and amplitude are determined by an emergent length scale λ over which compression can be accommodated. Furthermore, it is reasonable to expect that for these force densities, the emergent dynamics is controlled by a

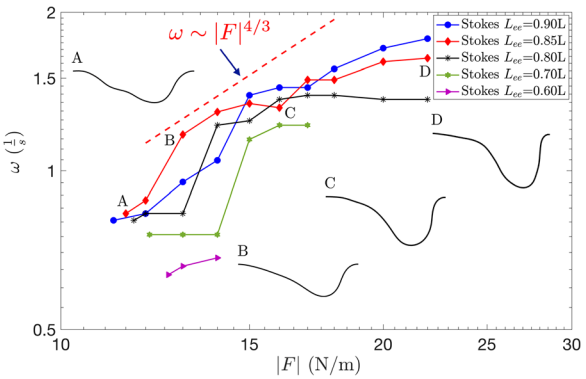

Fig. 6 Frequency of oscillations for rods as a function of $|F|$ for various values of L_{ee} when the fluid drag is of the Stokes [S] form. The form of the curves suggest possible transitions that may be related to the activation or deactivation of higher order mode shapes (typical shapes are shown alongside the curves). Sudden jumps in the frequency–force curve, for example from point A to point B, are due to the suppression of oscillation modes with smaller wavelength that also have higher energy level. Higher follower force densities yield increasingly steep shapes with localized curvature variations. When plotted on logarithmic axes, we find that the frequencies do not correlate well with the $\omega \sim |F|^{4/3}$ power law form for an inertialess cantilever with distributed follower forces, oscillating with a single dominant wavelength and frequency.

balance of activity and fluid dissipation with rod inertia playing a negligible role.

These observations can be used to estimate the frequencies for force densities larger than the critical value. When oscillations reach steady-state, the rate at which energy input into the system due to the action of the nonconservative follower forces balances the rate at which energy is dissipated by the fluid drag: in other words, power balance when steady, stable oscillations exist implies that *work done by follower forces/time ≈ dissipation rate*.

The rate at which active energy enters the system is proportional to the magnitude of the follower force (follower force density multiplied by a characteristic length) multiplied by a characteristic speed inherent to the oscillations. Since, for very large F or small L_{ee}/L, the effect of the slack (end-to-end distance L_{ee} becomes negligible with the oscillatory wavelength and amplitude determined, to leading order, by an emergent activity-dependent length scale λ over which compression can be accommodated. To estimate λ, we examine the shapes of the buckled rod relative to the base state noting that activity arises not from the prestressed values of f_3 but solely from $|F|$. Examining the moments acting on the whole rod and using dimensional analysis, we obtain

$$\lambda \sim \left(\frac{EI}{|F|}\right)^{\frac{1}{3}} \tag{17}$$

Thus, the rate at which active energy is generated (characteristic time scale here chosen as a period) is

$$\text{active energy} \sim (|F|\lambda)(\lambda\omega) \tag{18}$$

Energy dissipated by the drag force is proportional to the drag force, which, for the Morrison drag, is proportional to the velocity squared, times the velocity of oscillations; energy is then dissipated in the system following:

$$\text{dissipation} \sim (C_{\text{eff}}\lambda^2\omega^2)\lambda(\lambda\omega) \tag{19}$$

where C_{eff} captures the effective drag coefficient in the Morrison formula. Combining Eqs. (13)–(15), we find the following relationship

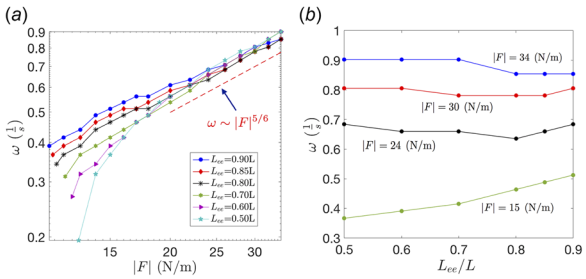

Fig. 7 (*a*) Frequency for the Morrison [M] drag plotted as a function of the force density $|F|$ plotted in logarithmic scales to illustrate two salient features—(i) as the follower force increases to values much larger than the critical values, the effect of the prestress diminishes, and (ii) the frequencies in the limit $|F| \gg F_{cr}$ scale roughly as $\omega \sim |F|^{5/6}$ consistent with our theoretical prediction. (*b*) Emergent frequency plotted as a function of the scaled end-to-end distance showing nonmonotonic behavior at fixed values of $|F|$. However, we note that as $|F|$ increases, the effect of the prestress and slack becomes decreasingly important for the range of L_{ee}/L investigated.

$$\omega^2 \sim \frac{|F|}{C_{\text{eff}}\lambda^2} \tag{20}$$

relating the frequency ω to the follower force density. Combining Eqs. (17) and (20) yields

$$\omega \sim \frac{1}{\sqrt{C_{\text{eff}}}}\left(\frac{|F|^{\frac{5}{2}}}{\text{EI}}\right)^{\frac{1}{3}} \sim |F|^{\frac{5}{6}} \tag{21}$$

Figure 7(*b*) shows that our simulations follow the scaling $\omega \sim |F|^{5/6}$ for $|F| \gg F_{\text{cr}}$ very well. The prediction that force–frequency curves converge to a universal curve for large values of the follower force, suggesting that prestress (L_{ee}) has a significant effect on response frequency close to the onset of oscillations. To evaluate quantitatively how the collection of curves follows 5/6 scaling law, we used least-square function approximation to fit a power law through the data for $|F| \geq 24\,\text{N/m}$. The results ($\omega \sim |F|^{0.8095}$) confirm the analytical relationship by 2.8% error.

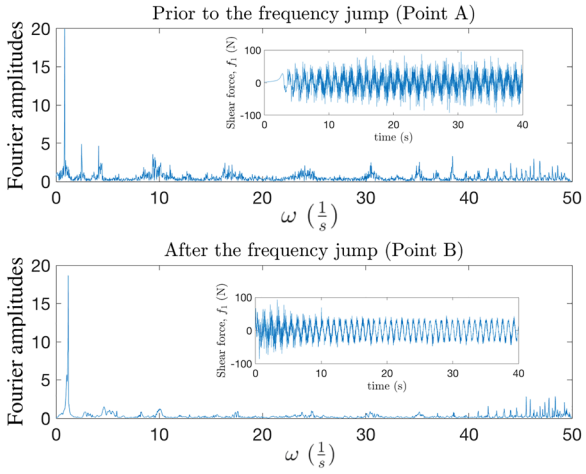

Fig. 8 Fourier transform (in the time domain) of the shear force at the midspan length of the rod subject to Stokes drag shows that higher harmonics are less pronounced as follower load, $|F|$, increases from $|F| = F_{cr} = 11.5\,\text{N/m}$ (point A) to $|F| = 13\,\text{N/m}$ (point B) for $L_{ee}/L = 0.85$. This correlates with the increase of steady-state frequency of the oscillations from point A to point B.

4 Conclusions

In this paper, we discussed the application of a computational rod model to analyze the buckling stability as well as the post-buckling oscillations of slender structures subjected to compressive follower loads. Simulations were first benchmarked with previous findings on magnitude of the critical buckling force for Beck's column. We focused on slender rods that maintain a straight shape corresponding to their stress-free state (i.e., having no intrinsic curvature and twist) with both ends clamped. By moving one end of the rod toward the other end, the structure undergoes buckling. This prestressed configuration was then subject to follower forces and the dynamics of the ensuing deformation investigated holding the inertia of the rod, geometry, and the fluid drag coefficients fixed. We found that beyond a critical value of distributed and compressive follower loads, the buckled shapes become unstable and oscillatory beating emerges. The magnitude of the critical follower load increases as the magnitude of the prestress in the structure increases. We also observed that frequency of the oscillations and the configuration of the rod are significantly influenced by the type of drag law used in modeling with Morrison drag inducing higher dissipation rate than Stokes drag. The frequency for the case of Morrison drag exhibits a power law dependence with exponent 5/6 on $|F|$ for forces much greater than the critical value at which oscillations are initiated. This exponent can be rationalized based on a power balance between the active energy pumped into the system by the nonconservative follower forces and dissipated due to fluid drag.

Our results provide a starting point to investigate the interplay between geometry, elasticity, dissipation, and activity toward designing bio-inspired multifunctional, synthetic structures to move and manipulate fluid at various length scales. While we have examined the fully stable nonlinear solutions in this work, the next step will be identifying and studying unstable as well as stable solutions in two and three dimensions using continuation methods adapted to time integrators, as done previously for liquid crystals and polymeric processes [35,36].

References

[1] Langthjem, M., and Sugiyama, Y., 2000, "Dynamic Stability of Columns Subjected to Follower Loads: A Survey," J. Sound Vib., **238**(5), pp. 809–851.
[2] Elishakoff, I., 2005, "Controversy Associated With the so-Called "Follower Forces": Critical Overview," ASME Appl. Mech. Rev., **58**(2), p. 117.
[3] Bolotin, V. V., 1999, "Dynamic Instabilities in Mechanics of Structures," ASME Appl. Mech. Rev., **55**(1), pp. R1–R9.
[4] Leipholz, H. H. E., 1980, *Stability of Elastic Systems/Horst Leipholz*, Sijthoff and Noordhoff/Alphen aan den Rijn, Alphen aan den Rijn, The Netherlands.
[5] Reut, V. I., 1939, "About the Theory of Elastic Stability," Odessa Institute of Civil and Communal Engineering, p. 1.
[6] Pfluger, A., 1950, *Stabilitatsprobleme Der Elastostatik*, Springer-Verlag, Berlin.
[7] Beck, M., 1952, "Die Knicklast Des Einseitig Eingespannten, Tangential Gedruckten Stabes," ZAMP Z. Fur Angew. Math. Phys., **3**(3), pp. 225–228.
[8] Païdoussis, M. P., 2016, *Fluid-Structure Interactions: Slender Structures and Axial Flow*, 2nd ed., Academic Press, London.
[9] Païdoussis, M. P., and Li, G. X., 1993, "Pipes Conveying Fluid: A Model Dynamical Problem," J. Fluids Struct., **7**(2), pp. 137–204.
[10] Wood, W. G., Saw, S. S., and Saunders, P. M., 1969, "The Kinetic Stability of a Tangentially Loaded Strut," Proc. R. Soc. A: Math., **313**(1513), pp. 239–248.
[11] Païdoussis, M., 1973, "Dynamics of Cylindrical Structures Subjected to Axial Flow," J. Sound Vib., **29**(3), pp. 365–385.
[12] Kang, B., and Tan, C. A., 2000, "Parametric Instability of a Leipholz Column Under Periodic Excitation," J. Sound Vib., **229**(5), pp. 1097–1113.
[13] Dreyfus, R., Baudry, J., Roper, M. L., Fermigier, M., Stone, H. A., and Bibette, J., 2005, "Microscopic Artificial Swimmers," Nature, **437**(7060), pp. 862–865.
[14] Babataheri, A., Roper, M., Fermigier, M., and Du Roure, O., 2011, "Tethered Fleximags as Artificial Cilia," J. Fluid Mech., **678**, pp. 5–13.
[15] Sasaki, Y., Takikawa, Y., Jampani, V. S. R., Hoshikawa, H., Seto, T., Bahr, C., Herminghaus, S., Hidaka, Y., and Orihara, H., 2014, "Colloidal Caterpillars for Cargo Transportation," Soft Matter, **10**(44), pp. 8813–8820.
[16] Patteson, A. E., Gopinath, A., and Arratia, P. E., 2016, "Active Colloids in Complex Fluids," Curr. Opin. Colloid Interface Sci., **21**, pp. 86–96.
[17] Chelakkot, R., Gopinath, A., Mahadevan, L., and Hagan, M. F., 2014, "Flagellar Dynamics of a Connected Chain of Active, Polar, Brownian Particles," J. R. Soc., Interface, **11**(92), p. 20130884.
[18] Vaziri, A., and Gopinath, A., 2008, "Cell and Biomolecular Mechanics in Silico," Nat. Mater., **7**(1), pp. 15–23.
[19] Gopinath, A., and Mahadevan, L., 2011, "Elastohydrodynamics of Wet Bristles, Carpets and Brushes," Proc. R. Soc. A, **467**(2130), pp. 1665–1685.
[20] Vaziri, A., Gopinath, A., and Deshpande, V. S., 2007, "Continuum-Based Computational Models for Cell and Nuclear Mechanics," J. Mech. Mater. Struct., **2**(6), pp. 1169–1191.
[21] Qin, B., Gopinath, A., Yang, J., Gollub, J. P., and Arratia, P. E., 2015, "Flagellar Kinematics and Swimming of Algal Cells in Viscoelastic Fluids," Sci. Rep., **5**, p. 9190.
[22] Maghsoodi, A., Chatterjee, A., Andricioaei, I., and Perkins, N. C., 2017, "Dynamic Model Exposes the Energetics and Dynamics of the Injection Machinery for Bacteriophage T4," Biophys. J., **113**(1), pp. 195–205.
[23] Maghsoodi, A., Chatterjee, A., Andricioaei, I., and Perkins, N. C., 2016, "A First Model of the Dynamics of the Bacteriophage T4 Injection Machinery," ASME J. Comput. Nonlinear Dyn., **11**(4), p. 041026.
[24] Goyal, S., 2006, "A Dynamic Rod Model to Simulate Mechanics of Cables and DNA," Ph.D. dissertation, University of Michigan, Ann Arbor, MI.
[25] Goyal, S., Perkins, N. C., and Lee, C. L., 2005, "Nonlinear Dynamics and Loop Formation in Kirchhoff Rods With Implications to the Mechanics of DNA and Cables," J. Comput. Phys., **209**(1), pp. 371–389.
[26] De Canio, G., Lauga, E., and Goldstein, R. E., 2017, "Spontaneous Oscillations of Elastic Filaments Induced by Molecular Motors," J. R. Soc. Interface, **14**(136), p. 20170491.
[27] Herrmann, G., and Bungay, R. W., 1964, "On the Stability of Elastic Systems Subjected to Nonconservative Forces," ASME J. Appl. Mech., **31**(3), pp. 435–440.
[28] Bayly, P. V., and Dutcher, S. K., 2016, "Steady Dynein Forces Induce Flutter Instability and Propagating Waves in Mathematical Models of Flagella," J. R. Soc. Interface, **13**(123), p. 20160523.
[29] Kirchhoff, G., 1859, "Uber Das Gleichgewicht Und Die Bewegung Eines Unendlich Dunnen Elastischen Stabes," J. Reine Angew. Math., **56**(56), pp. 285–343.
[30] Chung, J., and Hulbert, G. M., 1993, "A Time Integration Algorithm for Structural Dynamics With Improved Numerical Dissipation - the Generalized-Alpha Method," ASME J. Appl. Mech., **60**(2), pp. 371–375.
[31] Gobat, J. I., and Grosenbaugh, M. A., 2001, "Application of the Generalized-Alpha Method to the Time Integration of the Cable Dynamics Equations," Comput. Methods Appl. Mech. Eng., **190**(37–38), pp. 4817–4829.
[32] van der Heijden, G., Neukirch, S., Goss, V., and Thompson, J., 2003, "Instability and Self-Contact Phenomena in the Writhing of Clamped Rods," Int. J. Mech. Sci., **45**(1), pp. 161–196.
[33] Fatehiboroujeni, S., Palanthandalam-Madapusi, H. J., and Goyal, S., 2018, "Computational Rod Model With User-Defined Nonlinear Constitutive Laws," ASME. J. Comput. Nonlinear Dynam., **13**(10), p. 101006.
[34] Goyal, S., Perkins, N., and Lee, C. L., 2008, "Non-Linear Dynamic Intertwining of Rods With Self-Contact," Int. J. Non-Linear Mech., **43**(1), pp. 65–73.
[35] Anwar, Z., Gopinath, A., and Armstrong, R. C., 2012, "Systems Analysis of Hybrid, Multi-Scale Complex Flow Simulations Using Newton-GMRES," Rheol. Acta, **51**(9), pp. 849–866.
[36] Gear, C. W., Kaper, T. J., Kevrekidis, I. G., and Zagaris, A., 2005, "Projecting to a Slow Manifold: Singularly Perturbed Systems and Legacy Codes," SIAM J. Appl. Dyn. Syst., **4**(3), pp. 711–732.